



HAL
open science

Structure and properties of clay ceramics for thermal energy storage

Pierre-Marie Nigay, Ange Nzihou, Claire E. White, Winston O. Soboyejo

► **To cite this version:**

Pierre-Marie Nigay, Ange Nzihou, Claire E. White, Winston O. Soboyejo. Structure and properties of clay ceramics for thermal energy storage. *Journal of the American Ceramic Society*, 2017, 100 (10), pp.4748-4759. 10.1111/jace.15014 . hal-01630902

HAL Id: hal-01630902

<https://imt-mines-albi.hal.science/hal-01630902>

Submitted on 16 Jan 2019

HAL is a multi-disciplinary open access archive for the deposit and dissemination of scientific research documents, whether they are published or not. The documents may come from teaching and research institutions in France or abroad, or from public or private research centers.

L'archive ouverte pluridisciplinaire **HAL**, est destinée au dépôt et à la diffusion de documents scientifiques de niveau recherche, publiés ou non, émanant des établissements d'enseignement et de recherche français ou étrangers, des laboratoires publics ou privés.

Structure and properties of clay ceramics for thermal energy storage

Pierre-Marie Nigay^{1,2} | Ange Nzihou¹ | Claire E. White^{3,4} | Winston O. Soboyejo^{2,5}

¹Centre RAPSODEE, Ecole des Mines d'Albi, Albi, France

²Department of Mechanical Engineering, Worcester Polytechnic Institute, Worcester, Massachusetts

³Department of Civil and Environmental Engineering, Princeton University, Princeton, New Jersey

⁴Andlinger Center for Energy and the Environment, Princeton University, Princeton, New Jersey

⁵Department of Mechanical and Aerospace Engineering, Princeton University, Princeton, New Jersey

Correspondence

Pierre-Marie Nigay, Centre RAPSODEE, Ecole des Mines d'Albi, Albi, France.
Email: pmnigay@mines-albi.fr

Funding Information

This study was funded by Institut CARNOT Mines (CARNOT 2013).

Abstract

In this paper, the structure-property relationships of a clay ceramic with organic additives (biomass and biochar) are investigated to develop an alternative material for thermal energy storage. The firing transformations were elucidated using X-ray pair distribution function analysis, differential scanning calorimetry, and scanning electron microscopy. It was found that the biomass increased the porosity, which resulted in a decrease of the specific heat capacity. On the other hand, the biochar remained in the clay ceramic without any interaction with the clay matrix up to 950°C. The specific heat capacity of the clay ceramic increased from 1.20 to 1.49 kJ/kg·K for a 30 wt% addition of biochar. The clay ceramic with a 30 wt% addition of biochar also conserved a high flexural strength of 11.1 MPa compared to that of the clay ceramic without organic additives (i.e., 18.9 MPa). Furthermore, the flexural strength only decreased by 23% after 100 thermal cycles. The crack growth associated with the thermal fatigue was limited by crack bridging and crack trapping. Hence, the current results suggest that clay/biochar ceramics can be as efficient as molten salts in thermal energy storage with the added benefit of an ease of use in the physical form of bricks.

KEYWORDS

energy conversion, fatigue, phase transformations, R-curve, thermal properties

1 | INTRODUCTION

The production of electricity from renewable energy sources is expected to grow in the years ahead. The conversion of solar, wind, or biomass power is a sustainable way of reducing our modern dependency on fossil fuels. However, the use of renewables is still limited by the intermittency of the renewable energy sources.¹ For instance, solar-powered systems generate electricity during the daytime, while electricity is needed over 24 hours in a day.

Energy storage technologies have emerged to level the intermittent production of electricity from renewable energy sources. These technologies include electrochemical,² mechanical,³ or thermal energy storage.⁴ Thermal energy storage is based on a reversible transfer of heat, in the sensible or latent form,⁵ that does not require any production

of electricity. This makes thermal energy storage a low cost technology which is appropriate for many systems in the production of thermal energy.⁶

For sensible heat storage, materials are introduced in a container and heated. The amount of energy stored is proportional to the mass (i.e., porosity), the specific heat capacity, and the temperature increase of the storage materials. The temperature increase (charging) is usually performed by the circulation of warm air through the storage materials. Subsequently, energy can be reused (discharging) to warm a circulating flow of cool air. The charging/discharging rates are controlled by the shape of the storage materials in the case of a solid medium. In fact, a reduction of the thickness results in a greater exchange at the surfaces of the materials.⁷

Molten salts are widely used in thermal energy storage systems for their high specific heat capacities between 1.10

and 1.50 kJ/kg·K in liquid form.⁸ However, the utilization of liquid forms requires infrastructure with a complex system of tanks. Concrete is another attractive material for thermal energy storage. It has a low cost and relevant specific heat capacities of 0.95 kJ/kg·K.⁹ Nevertheless, the thermal degradation of concrete at temperatures greater than 500°C limits the utilization of concrete to low-temperature storage solutions.¹⁰

In contrast, many ceramic materials are stable up to temperatures of 1000°C.¹¹ The ceramic materials are also processed in the form of bricks that makes them convenient for thermal energy storage. However, most of the ceramic materials have low specific heat capacities in comparison with concrete or molten salts (0.87 kJ/kg·K).¹² The ceramic materials also remain expensive to produce compared to the other materials. Hence, the objective of this study is to investigate the structure-property relationship of a clay ceramic with organic additives (biomass and biochar) to develop an alternative material with a high specific heat capacity.

2 | MATERIALS AND EXPERIMENTAL METHODS

2.1 | Raw materials

The clay that was used in this study was extracted in the form of lumps from a clay quarry in the Toulouse area (France). The lumps of clay were ground into smaller lumps of around 3 mm using a rolling mill (LA 1527; Vicentini, Vicenza, Italy). The elemental composition of the clay, measured via X-ray fluorescence analysis (Epsilon 3-XL; PanAlytical, Almelo, the Netherlands), is given in Table 1. Note the predominance of silicon and aluminum oxides, with smaller amounts of calcium, iron, potassium and magnesium oxides.

The organic additives that were used in this study consisted of biomass and biochar. The biomass was produced by grinding a hard wood with a knife mill (Pulverisette 15, Fritsch, Idar-Oberstein, Germany), while the biochar was produced by pyrolysis of the biomass at 500°C. The elemental composition was measured using organic elemental analysis (Flash 2000; Thermo Fisher Scientific, Waltham, MA). The results of the organic elemental analyses are given in Table 2. They show that the organic additives are

TABLE 1 Elemental composition of the clay with the concentrations in silicon, aluminum, calcium, iron, potassium, and magnesium oxides

Sample	Concentration (wt%)					
	SiO ₂	Al ₂ O ₃	CaO	Fe ₂ O ₃	K ₂ O	MgO
Clay	57.1	14.5	8.9	6.2	3.0	2.2

composed of carbon, oxygen, and hydrogen with low concentrations of oxygen in the biochar compared to the biomass. The particle size of the organic additives was measured using laser granulometry (Mastersizer 3000; Malvern, Orsay, France). The results indicated that the biomass has an average particle size of 60 µm while the biochar has a smaller average particle size of 20 µm.

2.2 | Processing of the clay ceramic

The clay ceramic that was investigated in this study was produced from mixtures of clay, organic additives, and water. The mixtures were made in a kneading bowl by the mixing of clay with 5, 10, and 15 wt% of organic additives. The mixtures were kneaded for 5 minutes with a gradual addition of water up to 28 wt%. The mixtures were then extruded using a bench extruder (Reber, Corregioverde di Dosolo, Italy) composed of a pipe and a crank activated piston. The mixtures were pushed into the pipe and released across a die as clay blocks of 60 mm×30 mm×10 mm.

The clay blocks were subsequently dried at 25°C, 65°C, and 105°C for 24 hours in an electric oven (Memmert, Schwabach, Germany). Samples were then prepared from the dried blocks by polishing with P80, P120, P180, and P280 SiC abrasive papers (CarbiMet, Buehler, Uzwil, Switzerland). Finally, the samples were fired in a sealed box, with a nitrogen flow of 5 L/min, inside of a muffle furnace (K1253; Heraeus, Hanau, Germany). The samples that were used for the X-ray diffraction and pair distribution function analyses were fired at 30°C, 600°C, 800°C, or 1000°C. The other samples were fired under the same conditions at 950°C.

2.3 | Characterization of structure

The atomic structure of the clay ceramic was investigated using X-ray diffraction (XRD) analysis. The samples in powder form were loaded in a 1 mm diameter polyimide capillary, which was sealed at both ends with modeling clay. The capillaries were aligned on the capillary stage of the diffractometer (D8 Discover; Bruker, Madison, WI) and tested while spinning. The data were collected over a 2θ range of 2°-130°, with a step size of 0.05°, using a silver

TABLE 2 Elemental composition of the organic additives with the concentrations in carbon, hydrogen, oxygen, nitrogen, and sulfur elements

Sample	Concentration (wt%)				
	C	H	O	N	S
Biomass	49.5	6.8	42.4	0.2	0.0
Biochar	84.9	4.0	9.8	0.5	0.0

(Ag) radiation source ($\lambda=0.56 \text{ \AA}$). The scattering of the polyimide and modeling clay was subsequently removed by subtracting a baseline that was produced from the testing of an empty capillary which was yet sealed with modeling clay. Finally, the pair distribution functions of the samples were obtained by the application of a sine Fourier transform (Equation 1) to those total scattering functions $S(Q)$ in the PDFgetX2 software¹³ using a momentum transfer Q_{max} of 15 \AA^{-1} .

$$G(r) = \frac{2}{\pi} \int_{Q_{\text{min}}}^{Q_{\text{max}}} Q[S(Q)-1] \sin(Qr) dQ. \quad (1)$$

The weight loss of the clay ceramic was measured as a function of temperature, using thermogravimetric analyses (TGA). Unfired samples were analyzed in the form of 200 mg cylinders with a Q600 apparatus (TA Instruments, New Castle, DE). The data were collected from 30°C to 1100°C under a nitrogen flow at a heating rate of 5°C/min. The percentage of organic additives was determined by subtracting the weight loss of the clay ceramic without organic additives. This was done since the thermal behavior of the organic additives within the clay ceramic is different from that out of the clay ceramic.

The porosity of the clay ceramic was determined from the measurement of the bulk density and of the true density ($\varepsilon=1-\rho_{\text{Bulk}}/\rho_{\text{true}}$). The bulk density was measured using a balance and a caliper while the true density was measured by helium pycnometry analysis (Accupyc 1330; Micromeritics, Norcross, GA) after firing at the maximum temperature of 1100°C and grinding to eliminate the porosity.

The morphology of the organic additives and of the porosity within the clay ceramic was observed using scanning electron microscopy (XL30; Philips, Amsterdam, the Netherlands). The samples were embedded in a solidifying epoxy resin and polished before the imaging under backscattered imaging conditions.

2.4 | Determination of the thermal properties

The thermal properties of the clay ceramic were determined using a transitory plane source method (TPS 2500, Hot Disk AB, Gothenburg, Sweden). Duplicate samples of 30 mm×30 mm×5 mm were analyzed with a mica probe (3.189 mm radius) at 500°C. It involved the introduction of the facility in an electrical furnace (AET Technologies, Meylan, France). Following the test, an algorithm of the Thermal Constants Analyzer software (Hot Disk AB, Gothenburg, Sweden) was used to determine the volumetric heat capacity of the clay ceramic. The specific heat capacity was subsequently determined by dividing the volumetric heat capacity by the bulk density. The bulk density of the clay ceramic was obtained from measurements of the weight and of the dimensions using a balance and a caliper.

2.5 | Determination of the mechanical properties

The mechanical properties of the clay ceramic were measured by three-point bending. The measurements were performed using an Instron 8548 microtester (Instron, Norwood, MA) with a 50 mm span and a 500 N load cell. The specimens of 60 mm×10 mm×5 mm were loaded at a constant displacement rate of 1 mm/min until the onset of the fracture. The flexural strength (σ_f) was estimated from Equation 2, where F_{Max} is the maximum force, L is the loading span, B is the breadth, and H is the height of the specimens.¹⁴

$$\sigma_f = \frac{3F_{\text{Max}}L}{2BH^2}. \quad (2)$$

The fracture toughness/resistance-curve behavior of the clay ceramic was investigated using single edge notch bend (SENB) specimens. The SENB specimens with dimensions of 60 mm×10 mm×5 mm and notch depths of 2 mm (0.40-0.45 length-to-width ratio) were tested in the same Instron 8548 microtester (Instron, Norwood, MA) that was used for the measurements of the flexural strength. The specimens were loaded at a displacement rate of approximately 0.1 mm/min until pop-in was observed at the notch.

In-situ observations of cracking were carried out during the fracture experiments, using a microscope with a 5× magnification (MZ 8; Leica, Wetzlar, Germany). The loads were then increased in incremental stages to determine the resistance curves with procedures from the literature.¹⁵ The stress intensity factors (K_I) were obtained from Equation 3, where σ_f is the stress at the peak load, a is the crack length, and ($f(a/w)$) is a compliance function.¹⁶

$$K_I = f(a/W) \times \sigma_f \times \sqrt{\pi a}. \quad (3)$$

The underlying crack/microstructure interactions of the resistance-curve behavior were elucidated via *in-situ* optical microscopy (MZ 8, Leica) and *ex-situ* scanning electron microscopy (XL30, Philips) to guide the development of small/large-scale crack bridging and crack trapping models.

2.6 | Thermal reliability

The thermal reliability of the clay ceramic was investigated via three-point bending. The specimens with dimensions of 60 mm×10 mm×5 mm were tested after 0, 1, 10, and 100 thermal cycles. In fact, the thermal cycles were simulated by introduction and withdrawal of the specimens in a muffle furnace (K1253, Heraeus, Hanau, Germany) at 500°C. The residual strength of the specimens was determined, as described in Section 2.5.

The reason of the dependence of the residual strength on the number of thermal cycles was elucidated via scanning electron microscopy (XL30, Philips). The observations of the fracture surfaces of the three-point bending specimens were performed under secondary electrons (SE) imaging conditions. In this way, the lengths of the effective cracks could be measured to predict the residual strengths after thermal cycles.

3 | MODELING

3.1 | Structure

The modeling of the structure was based on the thermal behavior of the organic additives in the clay ceramic. The thermal behavior was modeled from the Van Krevelen diagram¹⁷ by reduction of the different domains in a temperature-based equation. The concentrations of carbon, oxygen, and hydrogen after the firing process were calculated as: $C+O+H=1$ with $O=x.C$ and $H=y.C$. These were also measured prior to the firing process using elemental analysis.

In this way, the weight percentages of each element that were released during the firing process were calculated as the differences between the concentrations before and after the firing process. The sum of the different weight percentages provided the weight loss of the organic additives at a given temperature. Hence, the percentage of organic additives in the clay ceramic ($\%_T$) was obtained from Equation 4, using the percentage of addition ($\%_{\text{addition}}$) and the weight loss ($\Delta m_{(T)}$) of the organic additives.

$$\%_{(T)} = \%_{\text{addition}} - (\%_{\text{addition}} \times \Delta m_{(T)}) \quad (4)$$

$$\varepsilon_{(T)} = \varepsilon_{\text{Clay}} + (\%_{\text{Addition}} - \%_{(T)}). \quad (5)$$

The porosity increase associated with the thermal degradation of the organic additives was regarded as equal to the difference between the percentage of organic additives before and after the firing process. In this way, the percentage of porosity at a given temperature ($\varepsilon_{(T)}$) was calculated by summing the porosity from the clay ($\varepsilon_{\text{Clay}}$ in Table 3) and the porosity increase from the organic additives as shown in Equation 5.

3.2 | Specific heat capacity

The specific heat capacity (c) of the clay ceramic was predicted using a rule-of-mixture approach (Equation 6). The predictions were obtained from the concentration ($\%_{\text{Elements}}$) and the intrinsic properties (C_{Elements}) of each element. The concentrations were measured by X-ray fluorescence analysis. On the other hand, the intrinsic properties of silicon, aluminum, calcium, iron, potassium, and magnesium elements of the clay were collected from the literature (given

in Table 3).¹⁸ A multiplicative factor of 2.16 was also used to transpose the intrinsic properties to the temperature of 500°C.¹⁹

$$c = \sum \%_{\text{Elements}} \times c_{\text{Elements}}. \quad (6)$$

For the organic additives, the concentrations were obtained from the estimates of the model described in the previous section. The intrinsic properties of carbon, oxygen, and hydrogen elements were also collected from the literature. They were subsequently transposed to the temperature of 500°C using a multiplicative factor of 1.14.²⁰ Finally, these values of the solid fraction were adapted to the clay ceramic using the previous estimates of the porosity.

3.3 | Mechanical strength

The mechanical strength of the clay ceramic was predicted using the damage model²¹ in Equation 7. The model determines the mechanical strength under a flexural loading (σ_f) from the damage of the clay ceramic (D) and the intrinsic strength of the clay (σ_{Clay}).

$$\sigma_f = (1 - D) \sigma_{\text{Clay}}. \quad (7)$$

The intrinsic strength of the clay was regarded as equal to 37.0 MPa. This value was obtained from the mechanical strength of the clay ceramic without organic additives. On the other hand, the damage of the clay ceramic was estimated from Equation 8,²² where $\%_{\text{Defects}}$ is the sum of the percentages of porosity and organic additives and ϕ is the median defect size.

$$D = \frac{2^\phi}{2^\phi - 1} \left[1 - \frac{1}{(1 + \%_{\text{Defects}})^\phi} \right]. \quad (8)$$

The median defect size relates the percentage of defects to their effective impact on the damage. In fact, the impact of the large pores was regarded as equal to that of a greater volume fraction of small pores. It was obtained from the particle size distribution of the organic additives with the estimates of the structure described in Section 3.1 (see Table 3).

3.4 | Fracture toughness

The fracture toughness/resistance curve (K_R) estimates of the clay ceramic were obtained from the sum of the initiation fracture toughness (K_I) and the toughening due to the observed crack-tip shielding mechanisms.²³ The crack-tip shielding mechanisms included small/large-scale bridging (K_B) and crack trapping (K_T) as shown in Equation 9.

$$K_R = K_I + \Delta K_B + \Delta K_T. \quad (9)$$

The toughening due to crack bridging was predicted by a small-scale approach²⁴ for crack extensions smaller than

TABLE 3 Inputs of the model equations for the specific heat capacity, the mechanical strength, the fracture toughness, and the thermal reliability

Model	Equations	Inputs	Origin	
Specific heat capacity	6	$c_{Si}=0.71$ kJ/kg·K $c_{Al}=0.90$ kJ/kg·K $c_{Ca}=0.65$ kJ/kg·K $c_{Fe}=0.45$ kJ/kg·K $c_K=0.76$ kJ/kg·K $c_{Mg}=1.02$ kJ/kg·K $c_C=0.71$ kJ/kg·K $c_O=0.92$ kJ/kg·K $c_H=14.30$ kJ/kg·K	Literature	
Mechanical strength	7, 8	$\sigma_{Clay}=37.0$ MPa $\varepsilon_{Clay}=23$ vol% $\phi_{Clay}=50$ μ m	Experiments	
Fracture toughness	9–12	$h_{[0;0]}=0.4980$ $h_{[0;1]}=2.4463$ $h_{[0;2]}=0.0700$ $h_{[0;3]}=1.3187$ $h_{[0;4]}=-3.0670$ $h_{[1;0]}=0.5416$ $h_{[1;1]}=-5.0806$ $h_{[1;2]}=24.3447$ $V_B=5$ vol% $\sigma_f=8.7$ MPa $R_{Biomass}=30$ μ m $L_{Biomass}=150$ μ m $R_{Biochar}=10$ μ m $L_{Biochar}=50$ μ m	$h_{[1;3]}=-32.7208$ $h_{[1;4]}=18.1214$ $h_{[2;0]}=-0.1927$ $h_{[2;1]}=2.55863$ $h_{[2;2]}=-12.6415$ $h_{[2;3]}=19.7630$ $h_{[2;4]}=-10.9860$	 Experiments
Thermal reliability	13, 14	$K_C=2.0$ MPa \sqrt{m} (Clay) $K_C=1.3$ MPa \sqrt{m} (Biomass) $K_C=1.6$ MPa \sqrt{m} (Biochar) $a_{Biochar}=0.7$ mm (1 cycle) $a_{Biochar}=0.9$ mm (10 cycles) $a_{Biochar}=2.3$ mm (100 cycles)	Experiments	

0.5 mm and by a large-scale approach²⁵ for crack extensions larger than 0.5 mm. The predictions of the small-scale bridging contribution (ΔK_{SSB}) were obtained from Equation 10, where V_B is the fraction of bridging ligaments, L is the distance from the crack-tip to the last unfractured ligament, x is the distance from the crack-tip, and σ_f is the strength of the bridging ligaments. The predictions of the large-scale bridging contribution (ΔK_{LSB}) were obtained from Equation 11, where $h(a,x)$ is a weight function (see Table 3).²⁶

$$\Delta K_{SSB} = V_B \sqrt{\frac{2}{\pi}} \int_0^L \frac{\sigma_f}{\sqrt{x}} dx \quad (10)$$

$$\Delta K_{LSB} = V_B \int_0^L \sigma_f h(a,x) dx \quad (11)$$

$$\Delta K_T = K_I \left[\left(1 - 2 \frac{R}{L} \right) + \left(2.1 + 4.8 \frac{R}{L} \right)^2 \frac{2R}{\%_{(T)}} \right] \quad (12)$$

The toughening due to crack trapping corresponds to the action of the particles of organic additives on crack propagation. The predictions of the crack trapping contribution were then obtained using the model²⁷ in Equation 12, where R is the radius of the particles, L is the distance between the particles, and $\%_{(T)}$ is the percentage of particles. It is important to note that the parameters of the crack-tip shielding models were all estimated from the optical and SEM images of the underlying crack/microstructure interactions.

3.5 | Thermal reliability

The residual strengths of the clay ceramics were predicted from observations of the cracks in the fractured three-point bending specimens after thermal cycles. The estimates were obtained using Equation 13, where σ_r is the residual strength of the clay ceramic, K_c is the critical fracture

toughness of the clay ceramic, F is the boundary correction factor of the effective crack, Q is the shape factor of the effective crack, and a is the length of the effective crack (see Table 3).²⁸

$$\sigma_r = \frac{K_c}{F \sqrt{\frac{\pi a}{Q}}} \quad (13)$$

The boundary correction factor that was used is a specific factor for semielliptical surface cracks. It is given by Equation 14, where M_1 , M_2 , M_3 , and g are curve fitting functions, f_ϕ is an angular function, f_w is a finite-width correction factor, t is the thickness of the plan, and a is the length of the effective crack.²⁹

$$F = \left[M_1 + M_2 \left(\frac{a}{t} \right)^2 + M_3 \left(\frac{a}{t} \right)^4 \right] g f_\phi f_w \quad (14)$$

The curve fitting functions that are used in Equation 14 were estimated from the ratio of the crack depth to the crack length (a/c). The estimates were all obtained for a ratio smaller than one. The determination of the curve fitting functions also included the parametric angle of the ellipse (ϕ). Note that the a/c ratio and the parametric angle of the ellipse were both estimated from the observations of the effective cracks.

4 | RESULTS AND DISCUSSION

4.1 | Structure

4.1.1 | Atomic structure

The X-ray pair distribution functions (PDFs) of the clay ceramic with a 15 wt% addition of biochar are shown in Figure 1. The atom-atom correlations indicate that the clay ceramic is composed of clay minerals (see Section 2.1) prior to firing (i.e., at 30°C). The tetrahedral sheets are represented by the Si–O correlation at 1.52 Å and the larger atom-atom distances at 4.24 and 7.44 Å.³⁰ The Al–O bonds of the octahedral sheets are also represented by the peaks at 1.92, 3.71, and 9.11 Å. Furthermore, the distances between the silicon and aluminum atoms (Si–Al) are observed in the PDF curve at 3.10, 5.24, and 8.10 Å.

The PDF curve obtained after firing at 600°C shows some changes in the intensities of the peaks. In fact, the clay minerals are subjected to dehydroxylation at temperatures between 450°C and 600°C.^{31,32} The transition from VI coordinated aluminum atoms to predominantly IV coordinated aluminum atoms decreases the intensities of the Al–O correlations at 1.92, 3.71, and 9.11 Å. The formation of tetrahedrally coordinated aluminum sites also results in an increase of the intensity in the original Si–O correlations at 1.52 Å, 4.24, and 7.44 Å.

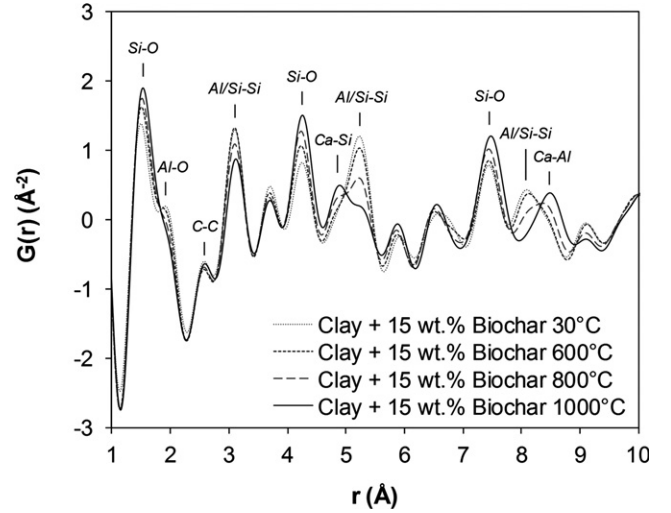


FIGURE 1 X-ray pair distribution function curves of the clay ceramic with a 15 wt% addition of biochar after firing at 30°C, 600°C, 800°C, and 1000°C

After firing at 800°C, the PDF curve shows some changes in the r spacing of the atom-atom correlations. The transformation of the Al–Si correlation at 8.10 Å into a Ca–Al correlation at 8.45 Å corresponds to a combination of aluminum atoms from the octahedral sheets with calcium atoms from calcite (CaCO_3) to form gehlenite ($\text{Ca}_2\text{Al}_2\text{SiO}_7$).³³ A combination of the silicon atoms from the tetrahedral sheets with the remaining atoms of calcium into wollastonite (CaSiO_3) is also visible in the PDF curve with a transformation of the Al–Si correlation at 5.24 Å into a Ca–Si correlation at 4.87 Å.³⁴ This incorporation of the octahedral and tetrahedral sheets of the clay minerals in gehlenite and wollastonite is completed after firing at 1000°C. The incorporation occurs via limited rearrangement of the silicon and aluminum atoms due to similar atom-atom distances between the clay minerals and these calcium aluminosilicates.

The PDF curves also show the presence of biochar with a C–C correlation of the aromatic cycles at 2.15 Å.³⁵ The intensity of the peak remains the same after firing at 30°C, 600°C, 800°C, and 1000°C. Hence, the biochar is not affected by the temperature due to firing in the nitrogen atmosphere. The r spacing of the C–C correlation also remains the same with the firing temperatures. This means that no interaction occurs between the biochar and the clay minerals during the firing process. In fact, the clay ceramic investigated in this study only corresponds to a matrix of calcium aluminosilicates enclosing organic additives.

4.1.2 | Percentage of organic additives

The dependence of the percentage of organic additives on the firing temperature of the clay ceramic is displayed in

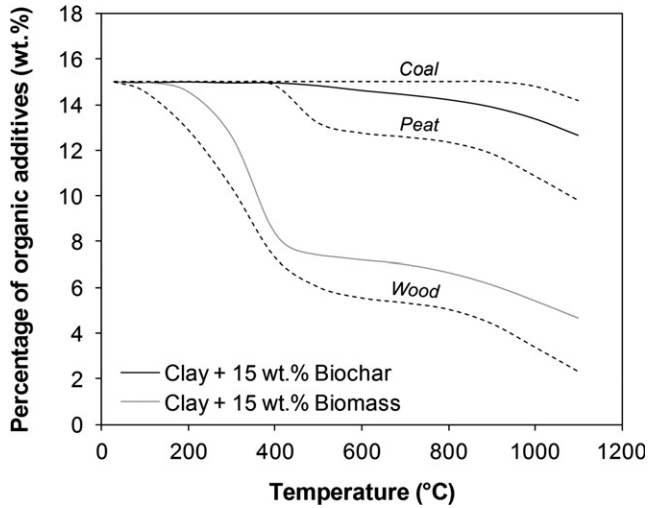


FIGURE 2 Dependence of the percentage of organic additive on the firing temperature of the clay ceramic with a 15 wt% addition of biomass and biochar in a nitrogen atmosphere

Figure 2. The biomass, composed of carbon, oxygen, and hydrogen elements transforms by pyrolysis³⁶ into CO, CO₂, CH₄, and H₂, whose release induces a porosity increase of the clay ceramic. But the biochar, which is composed of carbon and hydrogen elements, only transforms into CH₄ and H₂ at high temperatures. The clay ceramic with a 15 wt% addition of biochar has then a high percentage of organic additives of 14 wt% and a low porosity increase of 1 vol% after firing at the temperature of 950°C.

The thermal behavior of other organic additives, such as wood, peat, and coal is predicted from the Van Krevelen Diagram. The predictions obtained from the modeling also provide information for a larger addition of organic additives. In fact, the clay ceramic with a 30 wt% addition of biochar should contain up to 27 wt% of organic additives after firing at the temperature of 950°C.

4.1.3 | Morphology of organic additives

The SEM micrographs of the clay ceramic obtained after firing at 950°C are presented in Figure 3. The clay ceramic without organic additives has a heterogeneous structure of clay with pores and quartz particles. The pores correspond to the air retained in the clay ceramic during the extrusion process. These 10±2 μm pores are minor defects in the structure of the clay ceramic. In fact, the major defects of the structure remain the decohesions around the quartz particles with dimensions of 50±20 μm that are equivalent to the dimensions of the particles. These decohesions result from the larger shrinkage of quartz than that of the clay matrix during the β→α quartz inversion of the cooling.

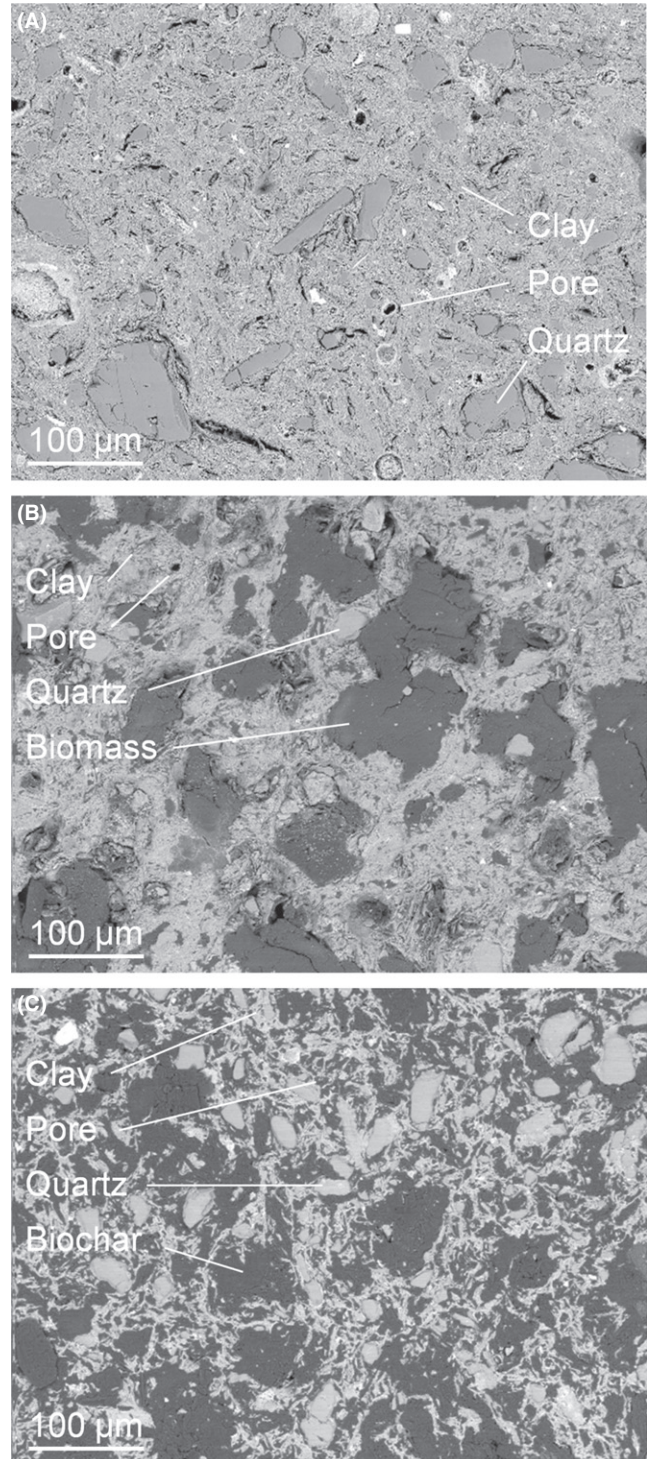


FIGURE 3 SEM micrographs of the clay ceramic (A), clay ceramic with a 15 wt% addition of biomass (B), clay ceramic with a 15 wt% addition of biochar (C), after firing at 950°C

The clay ceramic with a 15 wt% addition of biomass has a greater heterogeneity than that of the clay ceramic without organic additives. The 60 μm particles of the biomass appear as the largest defects of the clay ceramic after firing at a temperature of 950°C. However, the clay ceramic with a 15 wt% addition of biochar has a lower

heterogeneity than that of the clay ceramic without organic additives. The biochar particles are minor defects compared to the 50 μm decohesions around the quartz particles.

4.2 | Specific heat capacity

The dependence of the specific heat capacity of the clay ceramic on the percentage of organic additives is displayed in Figure 4. The clay ceramic without organic additives has a specific heat capacity of 1.20 ± 0.02 kJ/kg·K after a firing process at 950°C. This relatively high specific heat capacity compared to that of other ceramic materials³⁷ is attributed to the high concentration of alkali metals along with the relatively low percentage of porosity (i.e., 23 vol %). On the other hand, the relatively low uncertainty in the results of the specific heat capacity is due to the absolute nature of the measurements (transient plane source technique).

The biomass transform into gas, which the release induces a porosity increase of the clay ceramic during the firing process. The specific heat capacity of the clay ceramic is then decreased by 3% using a 15 wt% addition of biomass. However, the biochar is conserved in the clay ceramic during the firing process. The specific heat capacity of the clay ceramic is then increased by 12% in the case of a 15 wt% addition of biochar. Therefore, the clay ceramic with a 15 wt% addition of biochar has a specific heat capacity of 1.35 ± 0.02 kJ/kg·K after firing at 950°C. It is important to note that the conservation of the biochar prevents a significant decrease in the bulk density of the clay ceramic. Hence, the improvement of the volumetric heat capacity is equivalent to that of the specific heat capacity.

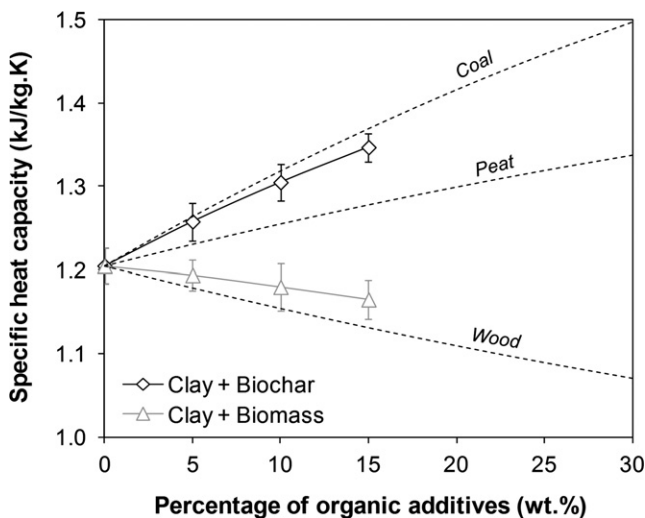


FIGURE 4 Dependence of the specific heat capacity of the clay ceramic on the percentage of organic additives after firing at 950°C

The modeling of the specific heat capacity also provides information for a larger addition of organic additives. In fact, the results obtained from the previous calculations of the elemental composition (after the firing process), along with values from the literature of the specific heat capacity of each element, indicate that the specific heat capacity of the clay ceramic should increase up to 1.49 kJ/kg·K for a 30 wt% addition of biochar. Such a high specific heat capacity is very promising for thermal energy storage. It means that the clay ceramic with a 30 wt% addition of biochar could be as efficient as molten salts with the added benefit of an ease of use in the physical form of bricks.

4.3 | Mechanical strength

The dependence of the mechanical/flexural strength on the percentage of organic additives is presented in Figure 5. The clay ceramic without organic additives has a mechanical strength of 18.9 ± 0.9 MPa after a firing process at 950°C. The mechanical strength depends on the sintering process and the bonding of the clay particles as well as the 50 μm defects around the quartz particles that initiate fracture.

The addition of organic additives in the clay ceramic induces a decrease in the mechanical strength. However, the severity of the decrease depends on the particle size of the organic additives. The 60 μm particles of the biomass correspond to the largest defects of the clay ceramic. The mechanical strength of the clay ceramic is then decreased by 37% in case of a 15 wt% addition of biomass. On the other hand, the 20 μm particles of the biochar represent minor defects in the clay ceramic. The mechanical strength is then only decreased by 16% using a 15 wt% addition of

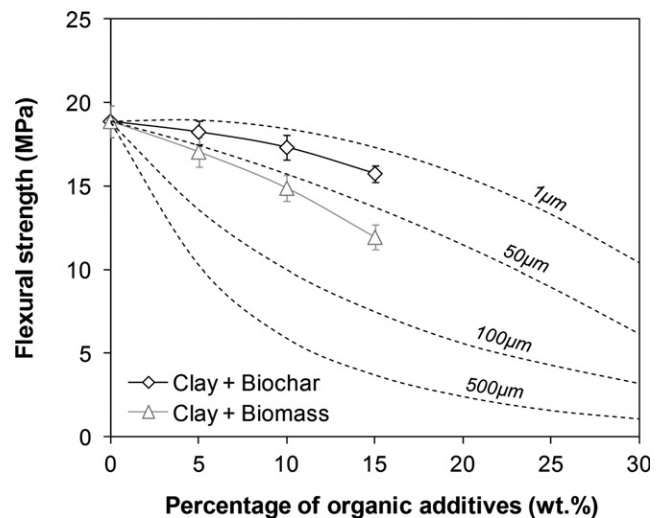


FIGURE 5 Dependence of the flexural strength of the clay ceramic on the percentage of organic additives after firing at 950°C

biochar. Therefore, the clay ceramic with a 15 wt% addition of biochar conserves a high mechanical strength of 15.8 ± 0.5 MPa after firing at 950°C . The dispersion in the mechanical strength of the clay ceramic (i.e., 0.5 MPa) is also reduced compared to that of the clay ceramic without organic additives (i.e., 0.9 MPa) due to the reduction in the heterogeneity of the structure.

The predictions of the damage model (Equations 7 and 8) are consistent with the results of the measurements. They also provide information for a larger addition of organic additives in the clay ceramic. In fact, the clay ceramic could have a mechanical strength of 11.1 MPa in the case of a 30 wt% addition of biochar.

4.4 | Resistance-curve behavior

The measured and predicted resistance-curve behavior are presented in Figure 6. The clay ceramic without organic additives has an initiation fracture toughness of $1.7 \text{ MPa}\sqrt{\text{m}}$. The fracture toughness of the clay ceramic also increases to $2.0 \text{ MPa}\sqrt{\text{m}}$ for a crack extension of 1.6 mm. This increase in the fracture toughness is due to toughening by crack bridging, as shown in Figure 7.

The addition of organic additives in the clay ceramic results in a decrease of the initiation fracture toughness. In fact, the particles of organic additives act as initiators of fracture in the clay ceramic. The $60 \mu\text{m}$ particles of the biomass decrease the initiation fracture toughness to $1.1 \text{ MPa}\sqrt{\text{m}}$ in the case of a 15 wt% addition. However, the initiation fracture toughness is only decreased to $1.3 \text{ MPa}\sqrt{\text{m}}$ for a 15 wt% addition of biochar with small $20 \mu\text{m}$ particles.

The clay ceramic with organic additives is also toughened by crack trapping, as observed in Figure 7. The

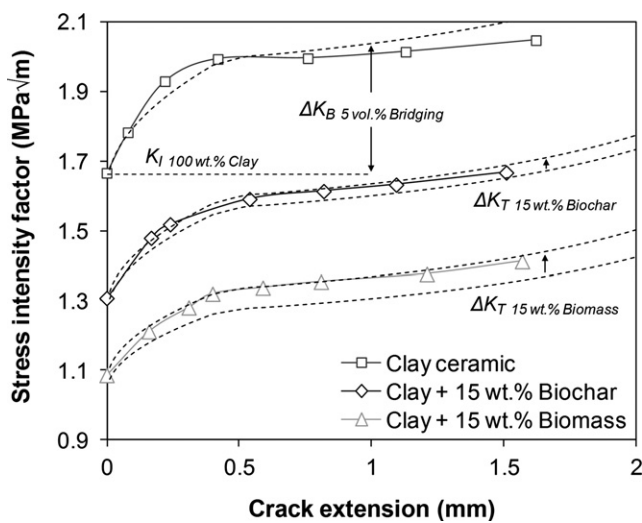


FIGURE 6 Resistance-curve behavior of the clay ceramic and of the clay ceramic with a 15 wt% addition of biomass and biochar after firing at 950°C

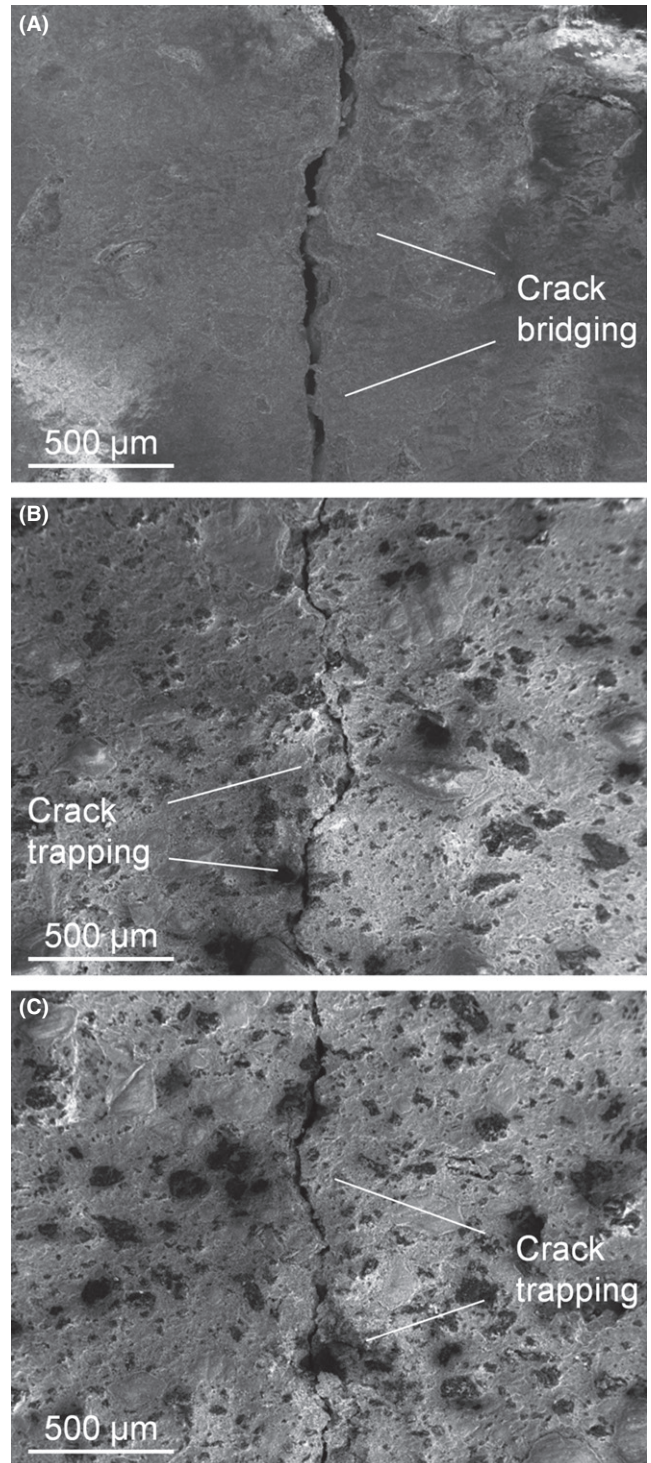


FIGURE 7 SEM micrographs of the crack-tip shielding mechanisms of the clay ceramic (A) and of the clay ceramic with a 15 wt% addition of biomass (B) and biochar (C) after firing at 950°C

combination of crack bridging and crack trapping mechanisms increases the fracture toughness of the clay ceramic with a 15 wt% addition of biomass to $1.5 \text{ MPa}\sqrt{\text{m}}$. On the other hand, the fracture toughness of the clay ceramic increases up to $1.7 \text{ MPa}\sqrt{\text{m}}$ using a 15 wt% addition of biochar.

4.5 | Thermal reliability

The dependence of the flexural strength on the number of thermal cycles is presented in Figure 8. The clay ceramic without organic additives has a flexural strength of 18.9 MPa after 0 thermal cycles. The flexural strength also decreases to 19.1, 17.6, and 14.8 MPa after 1, 10 and 100 thermal cycles. The decrease in the flexural strength is due to thermal fatigue. In fact, the thermal expansion mismatch between the constituents generates some cyclic stress concentration that lead to crack extension and fracture. This results in a 21% decrease of the flexural strength after 100 thermal cycles.

The addition of organic additives decreases the flexural strength before thermal cycling (see Section 4.3). The flexural strength also decreases with the thermal cycles, compared to that of the clay ceramic without organic additives, due to a lower initiation fracture toughness (see Section 4.4). However, the extra toughening (i.e., crack trapping) associated with the particles of organic additives also limits the crack extension, which contributes to a conservation of the flexural strength with the thermal cycles. The flexural strength only decreases by 26% after 100 thermal cycles in case of a 15 wt% addition of biomass. Similarly, the crack extension for the clay ceramic with a 15 wt% addition of biochar only results in a 23% decrease of the flexural strength after 100 thermal cycles.

It is important to note that the measured and predicted strengths of the clay ceramics are comparable after different thermal cycles. In fact, the results of both the measurements and the modeling indicate that the clay ceramic with a 15 wt% addition of biochar conserves a high residual strength of 12.1 MPa after 100 thermal cycles. This means

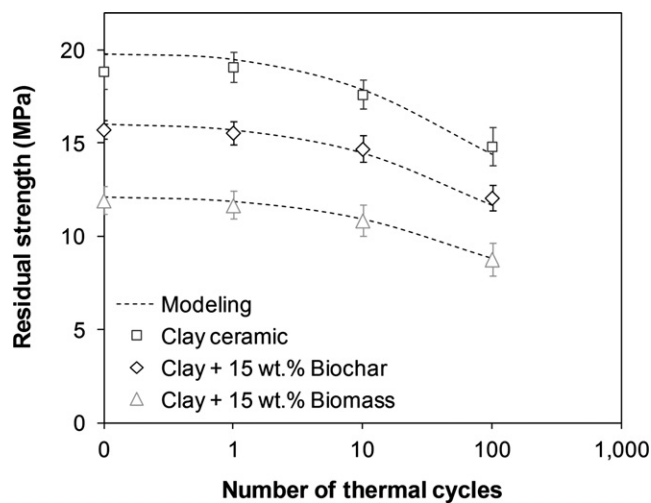


FIGURE 8 Dependence of the residual strength of the clay ceramic and of the clay ceramic with a 15 wt% addition of biomass and biochar on the number of thermal cycles at 500°C

that the clay/biochar ceramics can be considered as thermally reliable materials for a use in thermal energy storage.

4.6 | Implications

The implications of this research are significant for the use of ceramic materials in thermal energy storage. Thermal energy storage can be performed using ceramic materials or molten salts. However, molten salts remain the most widely used medium in thermal energy storage due to their high specific heat capacities between 1.10 and 1.50 kJ/kg·K.

This work shows that the specific heat capacities of ceramic materials can be improved up to 1.49 kJ/kg·K by the control of structure, via the addition of biochar. This means that 24% more energy can be stored in clay/biochar ceramics than in the same mass of conventional ceramics. The specific heat capacities of such ceramic materials are then comparable to the specific heat capacities of molten salts that are currently used in thermal energy storage.

Moreover, the clay/biochar ceramics in the physical form of bricks are much easier to use than molten salts. The clay/biochar ceramics are also thermally reliable materials with a significant strength after thermal cycles. This combination of specific heat capacity and flexural strength makes the clay/biochar ceramics one of the most appropriate materials for thermal energy storage. The valorization of biochar, which is a byproduct from the thermal conversion of wood, also minimizes the economical and environmental cost of the materials.

5 | CONCLUSIONS

In this paper, the structure-property relationship of a clay ceramic with organic additives (biomass and biochar) is investigated to develop an alternative material for thermal energy storage. Salient conclusions arising from this study are summarized below.

1. The atomic structure of the clay ceramic with organic additives transformed into calcium aluminosilicates during the firing process. However, the organic additives remained at the macroscopic scale without any interaction with the matrix at temperatures up to 1000°C.
2. The specific heat capacity decreased in the case of organic additives with high oxygen concentrations (biomass) due to a porosity formation. However, the conservation of the organic additives with low oxygen concentrations (biochar) resulted in an increase of the specific heat capacity up to 1.49 kJ/kg·K.
3. The flexural strength decreased in the case of organic additives with a large particle size (biomass) due to

stress concentration effects. However, the organic additives with small particles (biochar) resulted in a minor degradation of the flexural strength and fracture toughness. The extra toughening associated with the particles of organic additives also contributed to the conservation of the thermal reliability.

4. The clay ceramic with a 30 wt% addition of biochar had a comparable specific heat capacity to that of molten salts that are currently used in thermal energy storage. In addition, the clay/biochar ceramics offered the added benefit of an ease of use in the physical form of bricks.

ACKNOWLEDGMENTS

The authors acknowledge the CARNOT Mines Institute and the RAPSODEE Center at Ecole des Mines d'Albi for financial support. The authors are also grateful to the management and staff of the Department of Mechanical and Aerospace Engineering, and the Department of Civil and Environmental Engineering, and the Andlinger Center for Energy and the Environment at Princeton University, for their assistance with the research.

CONFLICT OF INTEREST

The authors declare that they do not have any conflict of interest.

REFERENCES

1. Barton JP, Infield DG. Energy storage and its use with intermittent renewable energy. *IEEE Trans Energy Convers.* 2004;19:441-448.
2. Dunn B, Kamath H, Tarascon JM. Electrical energy storage for the grid: a battery of choices. *Science.* 2011;334:928-935.
3. Rehman S, Al-Hadhrani LM, Alam MM. Pumped hydro energy storage system: a technological review. *Renew Sust Energ Rev.* 2015;44:586-598.
4. Ibrahim H, Ilinca A, Perron J. Energy storage systems—characteristics and comparisons. *Renew Sust Energ Rev.* 2008;12:1221-1250.
5. Kuravi S, Trahan J, Goswami DY, Rahman MM, Stefanakos EK. Thermal energy storage technologies and systems for concentrating solar power plants. *Prog Ener Combust.* 2013;39:285-319.
6. Aneke M, Wang M. Energy storage technologies and real life applications—a state of the art review. *Appl Energy.* 2016;179:350-377.
7. Li G, Zheng X. Thermal energy storage system integration forms for a sustainable future. *Renew Sust Energ Rev.* 2016;62:736-757.
8. Herrmann U, Kelly B, Price H. Two-tank molten salt storage for parabolic trough solar power plants. *Energy.* 2004;29:883-893.
9. John E, Hale M, Selvam P. Concrete as a thermal energy storage medium for thermocline solar energy storage systems. *Sol Energy.* 2013;96:94-204.
10. Willam K, Rhee I, Xi Y. Thermal degradation of heterogeneous concrete materials. *J Mater Civ Eng.* 2005;17:276-285.
11. Carty WM, Senapati U. Porcelain-raw materials, processing, phase evolution, and mechanical behavior. *J Am Ceram Soc.* 1998;81:3-20.
12. Laing D, Steinmann WD, Tamme R, Richter C. Solid media thermal storage for parabolic trough power plants. *Sol Energy.* 2006;80:1283-1289.
13. Qiu X, Thompson JW, Billinge SJL. PDFgetX2: a GUI-driven program to obtain the pair distribution function from X-ray powder diffraction data. *J Appl Cryst.* 2004;37:678-678.
14. Standard test methods for flexural properties of unreinforced and reinforced plastics and electrical insulating materials, D790-10. West Conshohocken, PA: American Society for Testing and Materials; 2010.
15. Soboyejo WO, *Mechanical Properties of Engineered materials.* New York, NY: CRC Press, Mechanical Engineering (Marcel Dekker);2002:414-455.
16. Standard test method for plane-strain fracture toughness of metallic materials, E399-90. West Conshohocken, PA: American Society for Testing and Materials; 1997.
17. van Krevelen DW. Graphical-statistical method for the study of structure and reaction processes of coal. *Fuel.* 1950;29:269-284.
18. Lide DR. *Handbook of Chemistry and physics.* Boca Raton, FL: CRC Press; 2009.
19. Wen H, Lu J, Xiao Y, Deng J. Temperature dependence of thermal conductivity, diffusion and specific heat capacity for coal and rocks from coalfield. *Thermochim Acta.* 2015;619:41-47.
20. Dupont C, Chiriac R, Gauthier G, Toche F. Heat capacity measurements of various biomass types and pyrolysis residues. *Fuel.* 2014;115:644-651.
21. Dean EA, Lopez JA. Empirical dependence of elastic moduli on porosity for ceramic materials. *J Am Ceram Soc.* 1983;66:366-370.
22. Sugarawa A, Yoshizawa Y. An investigation on the thermal conductivity of porous materials and its application to porous rock. *Austr J Phys.* 1961;14:469-480.
23. Evans AG, Faber KT. Crack-growth resistance of microcracking brittle materials. *J Am Ceram Soc.* 1984;67:255-260.
24. Budiansky B, Amazigo JC, Evans AG. Small-scale crack bridging and the fracture toughness of particulate-reinforced ceramics. *J Mech Phys Solids.* 1988;36:167-187.
25. Bloyer DR, Ritchie RO, Venkatesvara Rao KT. Fracture toughness and R-curve behavior of laminated brittle-matrix composites. *Metall Mater Trans A.* 1998;29:2483-2496.
26. Fett T, Munz D. Stress intensity factors and weight functions for one-dimensional cracks. Kernforschungszentrum Karlsruhe Institut für Materialforschung Rept. No. KFK 5290 December 1994.
27. Mower TM, Argon AS. Experimental investigations of crack trapping in brittle heterogeneous solids. *Mech Mater.* 1995;19:343-364.
28. Wang X. Stress intensity factors and weight functions for deep semi-elliptical surface cracks in finite-thickness plates. *Fatigue Fract Eng M.* 2002;25:291-304.
29. Newman JC, Raju IS. An empirical stress-intensity factor equation for surface crack. *Eng Fract Mech.* 1981;15:185-192.
30. Morandau AE, White CE. In situ X-ray pair distribution function analysis of accelerated carbonation of a synthetic calcium-silicate-hydrate gel. *J Mater Chem A.* 2015;3:8597-8605.
31. White CE, Provis JL, Proffen T, Riley DP, van Deventer JSJ. Density functional modeling of the local structure of kaolinite

- subjected to thermal dehydroxylation. *J Phys Chem A*. 2010;114:4988-4996.
32. Fernandez R, Martirena F, Scrivener KL. The origin of the pozzolanic activity of calcined clay minerals: a comparison between kaolinite, illite and montmorillonite. *Cem Concr Res*. 2011;41:113-122.
 33. Peters T, Iberg R. Mineralogical changes during firing of calcium-rich brick clays. *Am Ceram Soc Bull*. 1978;57:503-509.
 34. Cultrone G, Rodriguez-Navarro C, Sebastian E, Cazalla O, De La Torre MJ. Carbonate and silicate phase reactions during ceramic firing. *Eur J Miner*. 2001;13:621-634.
 35. Petkov V, Ren Y, Kabekkodu S, Murphy D. Atomic pair distribution functions analysis of disordered low-Z materials. *Phys Chem Chem Phys*. 2013;15:8544-8554.
 36. Di Blasi C. Modeling chemical and physical processes of wood and biomass pyrolysis. *Prog Energy Combust Sci*. 2008;34:47-90.
 37. Meffre A, Py X, Olives R, Bessada C, Veron E, Echegut P. High-temperature sensible heat-based thermal energy storage materials made of vitrified MSWI fly ashes. *Waste Biomass Valor*. 2015;6:1003-1014.